FUSED-PLANES: WHY TRAIN A THOUSAND TRI-PLANES WHEN YOU CAN SHARE?

Anonymous authors

Paper under double-blind review

ABSTRACT

Tri-Planar NeRFs enable the application of powerful 2D vision models for 3D tasks, by representing 3D objects using 2D planar structures. This has made them the prevailing choice to model large collections of 3D objects. However, training Tri-Planes to model such large collections is computationally intensive and remains largely inefficient. This is because the current approaches independently train one Tri-Plane per object, hence overlooking structural similarities in large classes of objects. In response to this issue, we introduce Fused-Planes, a novel object representation that improves the resource efficiency of Tri-Planes when reconstructing object classes, all while retaining the same planar structure. Our approach explicitly captures structural similarities across objects through a latent space and a set of globally shared base planes. Each individual Fused-Planes is then represented as a decomposition over these base planes, augmented with object-specific features. Fused-Planes showcase state-of-the-art efficiency among planar representations, demonstrating $7.2\times$ faster training and $3.2\times$ lower memory footprint than Tri-Planes while maintaining rendering quality. An ultralightweight variant further cuts per-object memory usage by 1875× with minimal quality loss.

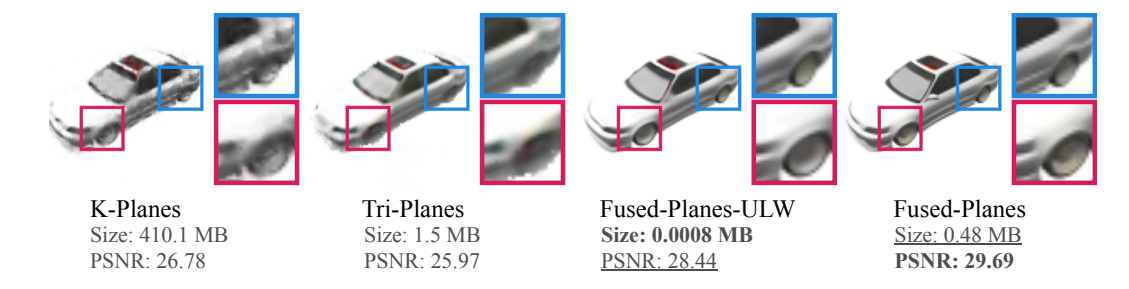


Figure 1: Comparison of planar representations under the same budget. Our method achieves the best rendering quality and the best memory footprint among planar representations when training large classes of 3D objects under a fixed time budget (7 minutes per object in this illustration). Fused-Planes-ULW designates the ultra-lightweight variant of Fused-Planes.

1 Introduction

Tri-planar representations (Chan et al., 2022; Fridovich-Keil et al., 2023) have recently driven significant progress in 3D computer vision, offering a unique advantage: they model 3D objects while remaining interpretable as 2D structures due to their planar format. This planarity makes them compatible with standard image-based models (e.g. CNNs), thereby unlocking new ways 2D vision models can be used for 3D tasks (Hong et al., 2024; Anciukevičius et al., 2023; Mercier et al., 2025). Given that such applications are inherently data-intensive, the need to train large collections of Tri-Planes for 3D reconstruction has become increasingly prevalent (Cardace et al., 2024; Shue et al., 2023; Ju & Li, 2025), and a costly preliminary step in 3D research (Liu et al., 2024; Wang et al., 2023, Sections 4.1 and 5). Yet, most existing methods overlook this costly 3D reconstruction step, focusing instead on the downstream tasks that planar representations enable. As such, using

planar representations for large-scale 3D reconstruction remains largely suboptimal in terms of resource efficiency, since existing methods train each Tri-Plane independently, ignoring the structural similarities that often exist across large object classes. This oversight leads to redundant computations and inefficient memory usage. As a result, constructing a dataset of Tri-Planes is currently unnecessarily computationally intensive.

In this work, we address the challenges associated with the computationally expensive task of large-scale 3D reconstruction using planar methods. We introduce Fused-Planes, a novel tri-planar representation that efficiently models large classes of 3D objects. Fused-Planes effectively reduces the resource costs associated with Tri-Planes by leveraging the structural similarities shared across multiple objects. Additionally, Fused-Planes retains the planar property of Tri-Planes that has enabled their integration into existing pipelines, and thus retains their compatibility with recent approaches.

First, our Fused-Planes split an object representation into two separate components: the first "Micro" component learns features specific to the object at hand; the second "Macro" component is a learned decomposition over a set of base planes, where each base plane encapsulates structural similarities across the class of objects we want to reconstruct. **Second**, we train Fused-Planes with a 3D-aware latent space (Schnepf et al., 2025), which provides a continuous and structured representation of objects, and accelerates the rendering and training of Fused-Planes.

The combination of these two cost-reducing components is essential. On the one hand, the latent space provides a more effective representation for disentangling object-specific details from class-level structural similarities, making it easier to capture these similarities with the set of base planes. On the other hand, the micro-macro decomposition is essential to eliminate the quality losses associated with using a latent space.

We conduct extensive experiments justifying these design choices and comparing our method with current planar representations when training on large classes of objects. Fused-Planes presents $7.2\times$ faster training than Tri-Planes, while requiring $3.2\times$ less memory footprint and retaining a similar rendering quality, thus establishing a new state-of-the-art in efficiency for planar scene representations. Moreover, an ultra-lightweight variant of Fused-Planes trades off minor rendering quality for substantial gains in memory footprint: $1875\times$ less than Tri-Planes. To the best of our knowledge, our work is the first to improve upon the resource efficiency of Tri-Planes.

2 Related Work

Tri-Planes. Tri-Planes (Chan et al., 2022) are widely used for modeling large collections of 3D objects and have attracted considerable attention due to their seamless integration with standard image-based models. In recent works, Tri-Planes are commonly used within a framework that involves solving two main tasks (Shue et al., 2023; Ju & Li, 2025). The first task is large-scale **3D reconstruction**, which consists of training Tri-Planes to properly model a large set of 3D objects. Once this prerequisite task is completed, the Tri-Planes can be reshaped into 2D image-like tensors, an operation made possible by their planar structure, making them easily integrable with image-based models. Once trained and reshaped, Tri-Planes are applied to a second, **targeted task**, in conjunction with a chosen image-based model. While recent studies have focused heavily on exploring diverse targeted tasks such as editing (Ki et al., 2025), classification (Cardace et al., 2024), generation (Liu et al., 2024), and feed-forward reconstruction (Wang et al., 2023), the first large-scale reconstruction task itself remains inefficient and sub-optimal, which has inspired our research direction. A more detailed discussion of works using Tri-Planes for downstream tasks can be found in appendix (Section A).

Other NeRF methods. Since NeRF (Mildenhall et al., 2020), methods like Instant-NGP (Müller et al., 2022), TensoRF (Chen et al., 2022), and 3D Gaussian Splatting (Kerbl et al., 2023) have advanced single-scene reconstruction. Yet, unlike Tri-Planes, their architectures cannot be reshaped into image-like tensors and are thus incompatible with image-based models. Even K-Planes (Fridovich-Keil et al., 2023), a multi-scale planar representation that surpasses Tri-Planes in fidelity, remains non-trivial to integrate with image-based models due to its multi-scale architecture. We thus mainly focus on Tri-Planes, as it is the only method that can be straightforwardly used with image-based models.

Our work aims to address the inefficiencies of large-scale 3D reconstruction with Tri-Planes. **First**, we design Fused-Planes to be a tri-planar *shared representation* that captures the structural similarities in object classes. **Second**, we train Fused-Planes as *latent NeRFs*, facilitating the learning of our shared representations. These design choices lead to substantial reductions in both training time and memory footprint.

Shared representations. Shared representations denote approaches that model multiple objects by utilizing common components. These representations encode an abstraction of a set of objects, effectively capturing dataset-level information such as structural similarities and differences among objects. For example, Jang & Agapito (2021) represent multiple objects of the same class within a single NeRF (MLP) by conditioning it on distinct latent codes for shape and appearance, which allows shape and appearance to be edited independently. Similarly, Schwarz et al. (2021); Niemeyer & Geiger (2021) adopt a shared representation implemented within a GAN framework, which enables the generation of novel objects and scenes. Notably, shared representations have been employed to reduce memory footprint when modeling multiple 3D objects. For instance, Singh et al. (2024) encode multiple scenes into a single NeRF using learned pseudo-labels, thereby reducing memory footprint. However, their method cannot scale beyond 20 scenes. Our work also utilizes shared representations for resource efficiency, but remains scalable to thousands of objects while reducing both memory footprint and training time. To the best of our knowledge, our method is the first to explicitly integrate shared representations with planar structures.

Latent NeRFs. Latent NeRFs involve training neural scene representations within the latent space of an image autoencoder, rather than directly using raw RGB images. Several recent works have utilized Latent NeRFs for 3D generation (Metzer et al., 2023; Seo et al., 2023; Ye et al., 2023; Chan et al., 2023), scene editing (Khalid et al., 2023; Park et al., 2024), and scene reconstruction (Aumentado-Armstrong et al., 2023) with improved quality. Recently, Schnepf et al. (2025) employed latent NeRFs to accelerate NeRF training. Their approach enables training various NeRF architectures within a 3D-aware latent space, resulting in substantial speed-ups but at the expense of a notable degradation in rendering quality. Our work builds upon Schnepf et al. (2025) by training our proposed Fused-Planes representation in a 3D-aware latent space. However, unlike Schnepf et al. (2025) who pre-train a generic latent space for all NeRF representations, we train the 3D-aware latent space jointly with our scene representations, which proves essential for preserving rendering quality. This improvement enables us to achieve substantial speed-ups without quality compromises.

3 METHOD

Our method efficiently reconstructs large collections of 3D objects using tri-planar representations. Section 3.1 presents our novel Fused-Planes representation, which splits an object representation into an object-specific "micro" component and a "macro" component derived from shared base representations. These base representations are trained on the entire dataset, allowing to capture global structural patterns shared by the objects being reconstructed. To achieve this, we train the set of Fused-Planes in a jointly learned 3D-aware latent space, which encodes the target objects in a compact and well-structured space, thereby facilitating the learning of shared patterns with our base planes. Section 3.2 describes our training procedure for Fused-Planes and the 3D-aware latent space. Figure 2 presents an overview of our method.

Notation. We denote $\mathcal{O} = \{O_1, ..., O_N\}$ a large set of N objects drawn from a common distribution. Each object $O_i = \{(x_{i,j}, c_{i,j})\}_{j=1}^V$ consists of V posed views. Here, $x_{i,j}$ and $c_{i,j}$ respectively denote the j-th view and camera pose of the i-th object O_i . We denote $\mathcal{T} = \{T_1, ..., T_N\}$ the set of Fused-Planes representations modeling the objects in \mathcal{O} .

3.1 Fused-Planes architecture.

Pre-requisite: Tri-Planes. Tri-Plane representations (Chan et al., 2022) are explicit-implicit scene representations enabling scene modeling in three axis-aligned orthogonal feature planes, each of resolution $K \times K$ with feature dimension F. To query a 3D point $x \in \mathbb{R}^3$, it is projected onto each of the three planes to retrieve bilinearly interpolated feature vectors. These feature vectors are

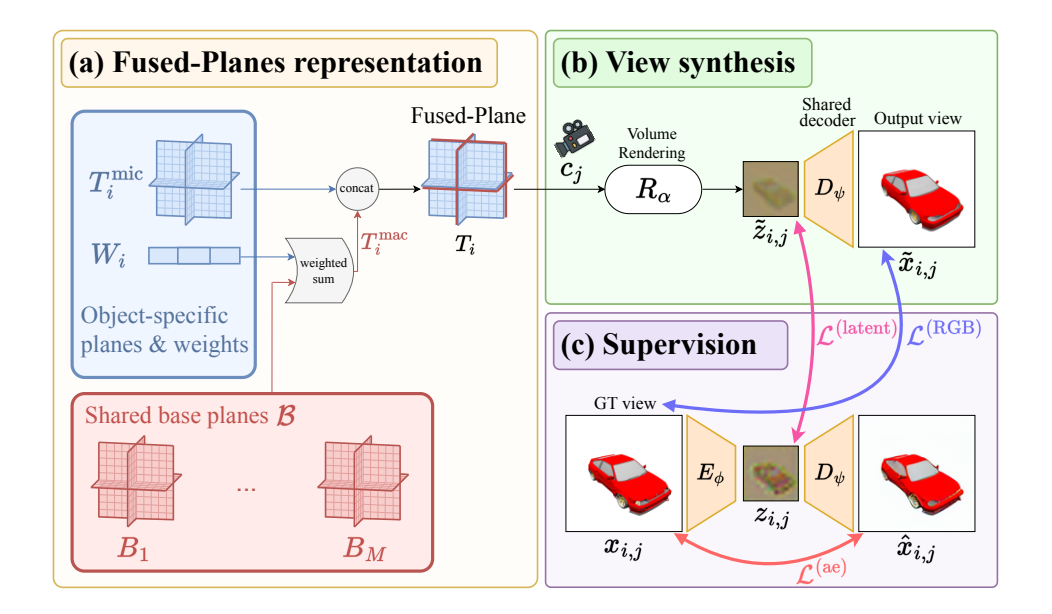


Figure 2: **Method overview.** A set of Fused-Planes $\{T_i\}$ reconstructs a class of 3D objects $\{O_i\}$ from their GT views $\{x_{i,j}\}$, where i and j respectively denote the object and the view indices. For clarity, only one Fused-Planes is shown. (a) Each Fused-Planes T_i is formed from a micro plane T_i^{mic} which captures object-specific information, and a macro plane T_i^{mac} computed via a weighted summation over a set of shared base planes \mathcal{B} . This base captures class-level information like structural similarities across objects. (b) View synthesis is performed in the latent space of an auto-encoder (E_ϕ, D_ψ) via classical volume rendering. The rendered latent image $\tilde{z}_{i,j}$ (low resolution) is decoded to obtain the output RGB view (high resolution). (c) The Fused-Planes components (i.e. T_i^{mic} , \mathcal{B} , W_i) and the autoencoder are supervised with three reconstructive losses.

then aggregated via summation and passed into a small neural network with parameters α to retrieve the color and density, which are then used for volume rendering (Kajiya & Von Herzen, 1984).

Notably, Tri-Planes can be represented as 2D structures by reshaping them into $K \times K$ images with 3F channels. As such, they can be seamlessly integrated in image-based pipelines. This planar property has been fundamental for their widespread adoption, and it is preserved in Fused-Planes.

Architecture of a Fused-Planes. Fused-Planes is a novel planar 3D representation that builds upon Tri-Planes. A Fused-Planes splits a planar representation into object-specific features, and class-level features, which allows to learn common structures across the large set of objects. Specifically, a Fused-Planes representation T_i of object O_i is composed of a "micro" plane $T_i^{\rm mic}$ integrating object-level information, and a "macro" plane $T_i^{\rm mac}$ that encompasses class-level information:

$$T_i = T_i^{\text{mic}} \oplus T_i^{\text{mac}} \,, \tag{1}$$

where \oplus concatenates two planar structures along the feature dimension. We denote by F^{mic} the dimensionality of local features in T_i^{mic} and by F^{mac} the dimensionality of global features in T_i^{mac} , with the total dimensionality of features in T_i being $F = F^{\mathrm{mic}} + F^{\mathrm{mac}}$.

The micro planes T_i^{mic} are object-specific, and are hence independently learned for every object. The macro planes T_i^{mac} represent globally captured information that is relevant for the current object. They are computed for each object from shared base planes $\mathcal{B} = \{B_k\}_{k=1}^M$ by the weighted sum:

$$T_i^{\text{mac}} = W_i \mathcal{B} = \sum_{k=1}^M w_i^k B_k \,, \tag{2}$$

where W_i are learned coefficients for object O_i . The base of planes $\{B_k\}_{k=1}^M$ is shared among objects and capture class-level structural similarities. With this approach, the number of micro planes is equal to the number of objects N, while the number of macro planes M is a constant

hyper-parameter. We take M>1 in order to capture diverse information, which our experiments showed to be beneficial for maintaining rendering quality, and $M\ll N$. Overall, decomposing Fused-Planes into micro and macro components reduces the number of trainable features per-object compared to traditional Tri-Planes, thus accelerating training and reducing total memory footprint.

Fused-Planes-ULW. We propose an ultra-lightweight (ULW) variant of our method with $F^{\rm mic} = 0$ (only macro planes), where we achieve substantial savings in memory footprint at the expense of a slight reduction in rendering quality.

3D-aware latent space. While Tri-Planes are traditionally used to model objects in the RGB space, we train Fused-Planes in the latent space of an image autoencoder, defined by an encoder E_{ϕ} and a decoder D_{ψ} . This is because a high-dimensional RGB space lacks structure, making it poorly suited for effectively capturing structural similarities. In contrast, a 3D-aware latent space (Schnepf et al., 2025) provides a structured and continuous encoding of the objects, which is, as proven by our ablations, more suited for disentangling structural similarities from object-specific details. Additionally, this latent space allows for a reduced rendering resolution, which alleviates the cost of volume rendering and contributes to accelerating our training. In practice, we train our 3D-aware latent space jointly with our Fused-Planes, which tailors it specifically for our decomposed object representation.

At inference, given a camera pose c_i , we render a latent Fused-Plane T_i as follows:

$$\tilde{z}_{i,j} = R_{\alpha}(T_i, c_j) , \qquad \qquad \tilde{x}_{i,j} = D_{\psi}(\tilde{z}_{i,j}) , \qquad (3)$$

where R_{α} is the Fused-Plane renderer with trainable parameters α , $\tilde{z}_{i,j}$ is the rendered latent image, and $\tilde{x}_{i,j}$ is the corresponding RGB decoded rendering.

3.2 TRAINING A LARGE SET OF FUSED-PLANES

This section outlines our training strategy to learn a large set of objects. In brief, we jointly train the set of Fused-Planes and the 3D-aware latent space. Figure 2 provides an overview of our pipeline.

Training a set of Fused-Planes jointly with the 3D-aware latent space. We train the set of Fused-Planes \mathcal{T} to reconstruct the set of objects \mathcal{O} from posed views. As described above, we conduct this training in a 3D-aware latent space in a joint manner. To do so, we adapt the 3D regularization losses from Schnepf et al. (2025). Note that our 3D-aware latent space differs from the one in (Schnepf et al., 2025), as it is subject to an additional training constraint coming from our micro-macro decomposition. This allows us to obtain a latent space that is not only 3D-aware, but also adapted to our Fused-Planes representations.

We supervise a Fused-Planes T_i and the encoder E_{ϕ} in the latent space with the loss $\mathcal{L}^{(\text{latent})}$:

$$\mathcal{L}_{i,j}^{(\text{latent})}(\phi, T_i) = \|z_{i,j} - \tilde{z}_{i,j}\|_2^2,$$
(4)

where $z_{i,j} = E_{\phi}(x_{i,j})$ is the encoded ground truth image, $\tilde{z}_{i,j} = R_{\alpha}(T_i, c_{i,j})$ is the rendered latent image, and $T_i = T_i^{\text{mic}} \oplus T_i^{\text{mac}}$. This loss optimizes the encoder parameters and the Fused-Planes parameters to align the encoded latent images $z_{i,j}$ and the rendering $\tilde{z}_{i,j}$. We also supervise T_i and the decoder D_{ψ} in the RGB space via $\mathcal{L}^{(\text{RGB})}$:

$$\mathcal{L}_{i,j}^{(RGB)}(\psi, T_i) = \|x_{i,j} - \tilde{x}_{i,j}\|_2^2,$$
(5)

where $x_{i,j}$ is the ground truth image, and $\tilde{x}_{i,j} = D_{\psi}(\tilde{z}_{i,j})$ is the decoded rendering. This loss ensures a good rendering quality when decoded to the RGB space, and finds the optimal decoder for this task. Finally, we adopt the reconstructive objective $\mathcal{L}^{(\text{ae})}$ supervising the auto-encoder:

$$\mathcal{L}_{i,j}^{(\text{ae})}(\phi,\psi) = \|x_{i,j} - \hat{x}_{i,j}\|_{2}^{2},$$
(6)

where $\hat{x}_{i,j} = D_{\psi}(E_{\psi}(x_{i,j}))$ is the reconstructed ground truth image.

Overall, our full training objective is composed of the three previous losses summed over \mathcal{O} to optimize the set of Fused-Planes \mathcal{T} , the encoder E_{ϕ} , and the decoder D_{ψ} :

$$\min_{\mathcal{T}, \phi, \psi} \sum_{i=1}^{N} \sum_{j=1}^{V} \lambda^{\text{(latent)}} \mathcal{L}_{i,j}^{\text{(latent)}}(\phi, T_i) + \lambda^{\text{(RGB)}} \mathcal{L}_{i,j}^{\text{(RGB)}}(\psi, T_i) + \lambda^{\text{(ae)}} \mathcal{L}_{i,j}^{\text{(ae)}}(\phi, \psi) , \qquad (7)$$

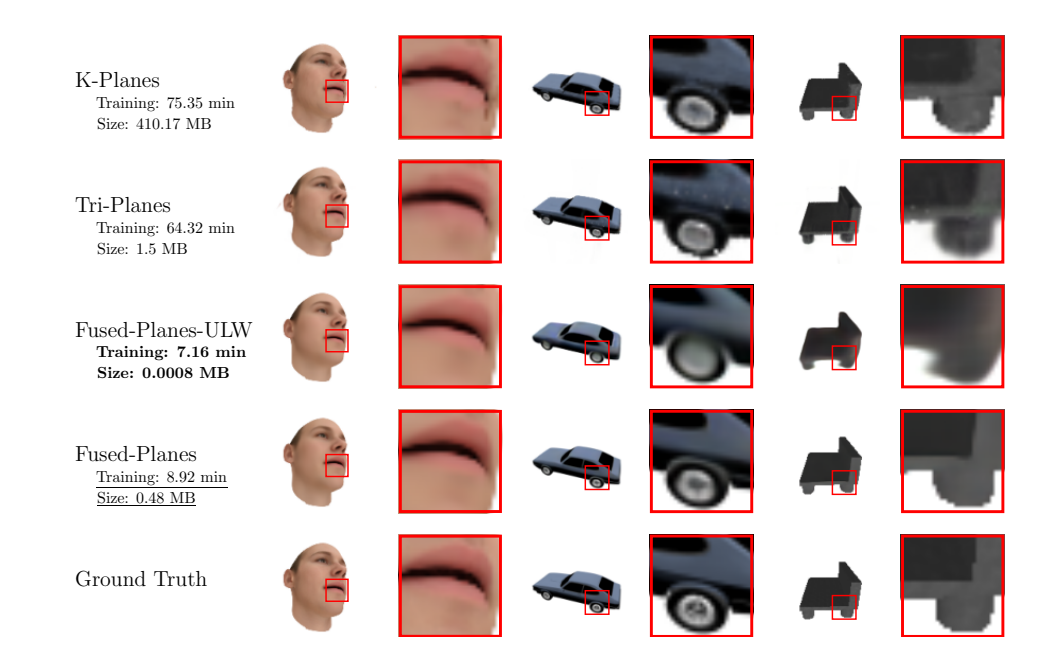


Figure 3: **Qualitative comparison.** We show comparisons of our method with other planar scene representations for NVS on held-out test views. Our method achieves the fastest training with the lowest memory footprint, while maintaining a comparable rendering quality.

where $\lambda^{(latent)}$, $\lambda^{(RGB)}$, and $\lambda^{(ae)}$ are hyper-parameters.

By the end of this training, the set of Fused-Planes $\mathcal T$ including the base planes $\mathcal B$ are learned and effectively model the objects in $\mathcal O$. Additional object representations could still be trained by utilizing the frozen shared components. For more implementation details, we refer the reader to the appendix (Section B and Algorithm 1).

4 EXPERIMENTS

Task. As discussed in Section 2, our goal is to reduce the resource costs of planar representations in large-scale 3D modeling. To establish the practical utility of our representation, it must satisfy two criteria: (i) accurately represent the types of 3D objects typically modeled with Tri-Planes, and (ii) demonstrate competitive resource efficiency relative to the Tri-Planes baseline. Regarding 3D modeling performance, we adopt the standard evaluation protocol for 3D representations and assess our method on the task of 3D reconstruction via Novel View Synthesis (NVS). For resource efficiency, we measure the per-object training time and memory footprint when modeling large object classes.

Evaluation Protocol To evaluate the NVS quality of the learned objects, we compute the PSNR (\uparrow) , SSIM (\uparrow) and LPIPS (Zhang et al., 2018, \downarrow) between never-seen reference views and corresponding NVS views. To evaluate the resource requirements, we report per-object training time, per-object memory footprint (excluding shared components), and total memory footprint. Training times are measured using a single NVIDIA L4 GPU.

Baselines. We compare Fused-Planes with three distinct lines of work. **First,** the central comparison is with planar scene representations, specifically Tri-Planes (Chan et al., 2022) and K-Planes (Fridovich-Keil et al., 2023), the only current works having planar structures. Tri-Planes is our baseline architecture and hence is our main point of comparison. K-Planes extend Tri-Planes to improve rendering quality by utilizing multi-scale planes, sacrificing on memory footprint, and most importantly the explicit 2D structure, as multi-scale planes cannot be directly reshaped into a single 2D structure. **Second,** we compare Fused-Planes with works utilizing shared representations. From this category, we consider CodeNeRF (Jang & Agapito, 2021), a recent non-planar method utilizing a

Table 1: **Comparison with planar methods.** Fused-Planes reduces the quality gap between Tri-Planes and K-Planes, while requiring three orders of magnitude less memory footprint, and having a significantly faster training, thus establishing a new state-of-the-art in efficiency for modeling large object classes with planar representations.

	Planar	Training	Size	Shaj	eNet dat	asets	F	Basel Face	es
	1 Idildi	(min)	(MB)	PSNR	SSIM	LPIPS	PSNR	SSIM	LPIPS
K-Planes (Fridovich-Keil et al., 2023) Tri-Planes (Chan et al., 2022)	/	75.35 64.32	410.17 1.50	30.88 28.15	0.956 0.919	0.043 0.121	40.23 36.47	0.991 <u>0.980</u>	0.005 0.013
Fused-Planes-ULW (ours) Fused-Planes (ours)	1	7.16 8.96	0.0008 0.48	29.02 30.47	0.937 0.957	0.092 0.042	33.96 <u>37.24</u>	0.955 0.973	0.010 <u>0.006</u>

Table 2: **Comparison with methods using shared representations.** Fused-Planes demonstrates more favorable NVS quality and per-object resources requirements compared to CodeNeRF.

	Planar	Training	Size	ShapeN	Vet datase	ets (avg)	I	Basel Face	es
	Tianai	(min)	(MB)	PSNR	SSIM	LPIPS	PSNR	SSIM	LPIPS
CodeNeRF (Jang & Agapito, 2021)	×	14.96	0.0026	28.34	0.930	0.121	35.46	0.972	0.010
CodeNeRF-A (our adaptation)		9.54	0.0026	26.99	0.915	0.126	35.44	0.971	0.010
Fused-Planes-ULW (ours)	/	7.16	0.0008	29.02	0.937	0.092	33.96	0.955	0.010
Fused-Planes (ours)		8.96	0.48	30.47	0.957	0.042	37.24	0.973	0.006

Table 3: **Report of standard NeRF methods.** To provide the reader with a broader perspective, we report the metrics of other well-established NeRF methods. As discussed, these methods do not share the same architectural versatility as planar methods and are designed for different objectives.

	Planar	Training	Size	ShapeN	Vet datase	ets (avg)	F	Basel Face	es
	1 Ianai	(min)	(MB)	PSNR	SSIM	LPIPS	PSNR	SSIM	LPIPS
Vanilla-NeRF (Mildenhall et al., 2020)	Х	636.8	22.00	35.85	0.977	0.027	42.91	0.996	0.001
Instant-NGP (Müller et al., 2022)	X	7.52	189.13	34.06	0.973	0.022	36.54	0.981	0.009
TensoRF (Chen et al., 2022)	X	68.93	208.32	36.74	0.985	0.013	40.66	0.991	0.004
3DGS (Kerbl et al., 2023)	X	9.37	27.66	32.95	0.975	0.043	43.06	0.995	0.002
Fused-Planes-ULW	✓	7.16	0.0008	29.02	0.937	0.092	33.96	0.955	0.010
Fused-Planes	✓	8.96	0.48	30.47	0.957	0.042	37.24	0.973	0.006

shared NeRF conditioned by latent vectors. We also compare with CodeNeRF-A, our adaptation of CodeNeRF designed to improve efficiency (more details in Section E). Note that we do not compare with C3-NeRF (Singh et al., 2024) as their approach does not scale beyond 20 scenes. **Third,** and to provide the reader with a larger perspective, we report the performance of other well-established non-planar scene representations (Mildenhall et al., 2020; Müller et al., 2022; Chen et al., 2022; Kerbl et al., 2023), using their Nerfstudio (Tancik et al., 2023) implementations. While these methods are designed to model scenes *individually* with high fidelity, they are not as readily integrable with image-based models as planar methods, and therefore lack their architectural versatility. As such, they are not our primary point of comparison, but are included to provide broader context.

Datasets & Experimental Details. We evaluate our method on large-scale 3D data. Consistently with Tri-Planes and CodeNeRF, we use ShapeNet (Chang et al., 2015), from which we take four categories: Cars, Furniture, Speakers and Sofas. Additionally, we adopt the large-scale front-facing Basel-Face dataset (Paysan et al., 2009). More dataset details can be found in the Section C. In our experiments, we train a set of Fused-Planes to reconstruct N=2000 objects. We use planes of dimensionality $K \times K \times F$, where K=64 and F=32 for all planar representations. For Fused-Planes, we take $F^{\rm mic}=10$, $F^{\rm mac}=22$, and M=50. For Fused-Planes-ULW, we take $F^{\rm mic}=0$, $F^{\rm mac}=32$, and M=50. We detail our hyper-parameters in Section F. We adopt the pre-trained VAE from Stable Diffusion (Rombach et al., 2022) as initialization for our VAE.

4.1 RESULTS

Main results appear in Tables 1 to 3 and Figures 1 and 3. Detailed results are available in Section D.

Table 4: **Ablation study.** Comparison of NVS quality and per-object resource costs for different ablations of our method on ShapeNet Cars. Fused-Planes outperforms all of its ablations. Fused-Planes-ULW trades off minor NVS quality for substantial savings in memory footprint.

	Latent Space	Micro Planes	Macro Planes	Training (min)	Size (MB)	PSNR	SSIM	LPIPS
Fused-Planes $(M = 1)$	✓	✓	√	8.48	0.48	27.69	0.942	0.042
Fused-Planes (Micro)	✓	✓	X	12.84	1.50	27.64	0.941	0.040
Fused-Planes (RGB)	X	✓	✓	63.52	0.48	27.71	0.942	0.044
Tri-Planes	X	✓	X	64.08	1.50	28.56	0.953	0.035
Fused-Planes-ULW	/	Х	/	7.16	0.0008	27.51	0.935	0.063
Fused-Planes	✓	✓	✓	8.92	0.48	28.64	0.950	0.037

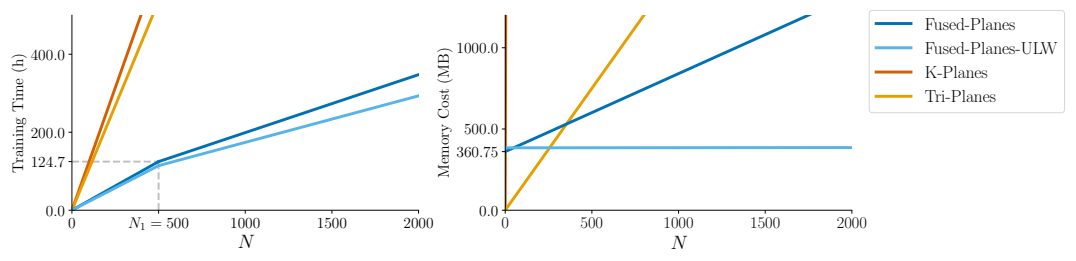


Figure 4: Scaling the number of objects using planar methods. Evolution of the total training time (left) and total memory footprint (right) when scaling the number of objects (N). As K-Planes is barely visible (right), we present in Figure 6 a magnified version of the memory cost plot.

Compared to other **planar scene representations** (Figure 1 and Table 1), Fused-Planes exhibits a significant reduction in resource costs, demonstrating $7.2\times$ faster training and $3.2\times$ less memory footprint than Tri-Planes, and $8.4\times$ faster training and $854\times$ less memory footprint than K-Planes. It improves rendering quality over Tri-Planes while reducing the gap with K-Planes, but without K-Planes' orders-of-magnitude higher memory cost or multi-scale complexity. Fused-Planes-ULW trades off minor rendering quality for substantial gains in memory footprint: one object requires $1875\times$ less memory footprint than Tri-Planes, and $512\,000\times$ less memory footprint than K-Planes. Furthermore, Figure 4 illustrates the evolution of the resource requirements as the number of objects increases. Moreover, a detailed breakdown of the memory footprint of Fused-Planes can be found in the appendix (Table 7). All in all, Fused-Planes establishes a new state-of-the-art in terms of resource efficiency for planar scene representations.

As for other methods utilizing **shared representations** (Table 2), Fused-Planes and Fused-Planes-ULW showcase up to $2\times$ faster training times, and an improved rendering quality. Fused-Planes-ULW also requires less memory footprint per-object.

For broader context, we report results on other well-established **non-planar** NeRF methods (Table 3 and Figure 5). Fused-Planes, like all other planar representations, showcases lower rendering quality, which is an acceptable trade-off as planar methods have a different primary objective (Section 2).

4.2 ABLATIONS

To justify our design choices, we present an ablation study of our method (Table 4). "Fused-Planes (M=1)" reduces the shared base planes \mathcal{B} to a single plane. It demonstrates a slight degradation of quality compared to Fused-Planes, highlighting the necessity for *a set* of base planes. "Fused-Planes (Micro)" eliminates the Macro component of Fused-Planes (i.e. $F^{\rm mac}=0$), and therefore the shared components. It exhibits lower quality compared to Tri-Planes, which is in line with the degradations seen in Schnepf et al. (2025) for latent NeRFs. In contrast, our full model avoids such issues, underscoring the benefits of shared representations within the latent space, both in quality and memory efficiency. "Fused-Planes (RGB)" ablates the latent space and trains Fused-Planes in RGB space. It exhibits lower quality compared to Tri-Planes, and to our full model. Therefore, it shows the necessity of the latent space for making shared representations work effectively. It also highlights the speed improvements enabled by the latent space. "Tri-Planes" is equivalent to ablating both the latent space and macro planes, which presents significantly higher resource costs and similar quality.

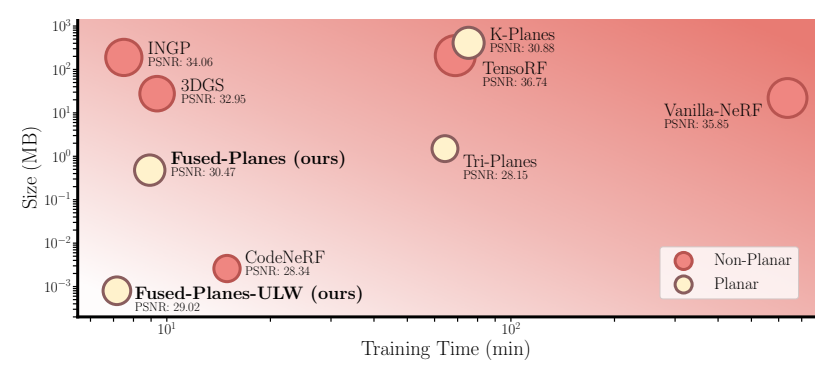


Figure 5: **Resource costs overview.** To reconstruct a large class of objects, our method presents the lowest per-object training time and memory footprint among all planar representations, while maintaining a similar rendering quality. Circle sizes represent the NVS quality.

In summary, our ablations show that both the latent space and shared representations are needed *concurrently* to avoid quality degradations and minimize resource costs.

4.3 LIMITATIONS

Tri-Planes are well-suited for object-centric scenes. However, they exhibit limitations in capturing fine details and handling unbounded scenes, which are characteristic of real-world environments. As such, Tri-Planes cannot be used to reconstruct scenes such as the ones used in the NeRF paper (Mildenhall et al., 2020) or in the Mip-NeRF 360 dataset (Barron et al., 2022). More precisely, to capture fine details, one would need to greatly increase the resolution of each of the Tri-Planes feature grids, leading to significant increases in memory footprint and computation, which undermines the compactness that makes Tri-Planes attractive. Moreover, Tri-Planes assume that the scene fits in a bounded volume, which complicates the modeling of distant backgrounds often present in real scenes. Some methods (Wu et al., 2024; Lee et al., 2024; Yan et al., 2024) sidestep these limitations by using tricks like utilizing multiple Tri-Planes for large scenes or by modeling only density and relying on other tools for textures. These approaches are beyond this paper's scope.

Since our method adopts the same architecture as Tri-Planes, it also inherits their limitations. Even so, Tri-Planes have been widely adopted (Section 2), as their planar design provides practical advantages despite these drawbacks. Our contribution advances this line of work by proposing a more efficient way to train planar methods at large-scales, while improving the quality of Tri-Planes.

Fused-Planes is effective at capturing structural similarities within an object class. To model multiple classes exhibiting large visual variations, multiple instances of Fused-Planes would be needed (i.e. multiples sets of shared based planes). Nonetheless, this is acceptable as current datasets categorize 3D assets by classes (as is the case for ShapeNet in our experiments), making Fused-Planes easily adaptable to such contexts, with the same efficiency gains. Alternatively, objects could be classified into classes rather easily with recent classification methods. We leave concurrent multi-class modeling with Fused-Planes as a direction of future work.

5 Conclusion

In this work, we introduced Fused-Planes, a novel planar object representation that advances the state of the art in resource-efficient planar 3D modeling and reconstruction of large object classes. This is achieved by shifting away from the traditional approach of reconstructing each object in isolation, and instead exploiting the shared structural similarities within object classes using shared base representations in a specially designed latent space. We showed that Fused-Planes significantly reduces required resources compared to current planar representation, while maintaining rendering quality. Given the recurrent challenges associated with training large-scale planar scene representations, we hope that our contribution will facilitate this task, and make research in image-based models for 3D applications more accessible.

REPRODUCIBILITY STATEMENT

We have taken several measures to ensure the reproducibility of our findings. The paper includes the necessary implementation details and hyperparameter settings in order to reproduce our results. Additionally, the complete source code is included in the supplementary materials of this submission and will be released as open-source upon publication. Together, these resources should allow researchers to fully reproduce and extend our findings.

REFERENCES

- Titas Anciukevičius, Zexiang Xu, Matthew Fisher, Paul Henderson, Hakan Bilen, Niloy J. Mitra, and Paul Guerrero. RenderDiffusion: Image Diffusion for 3D Reconstruction, Inpainting and Generation. In *Proceedings of the IEEE/CVF Conference on Computer Vision and Pattern Recognition (CVPR)*, pp. 12608–12618, June 2023.
- Tristan Aumentado-Armstrong, Ashkan Mirzaei, Marcus A Brubaker, Jonathan Kelly, Alex Levinshtein, Konstantinos G Derpanis, and Igor Gilitschenski. Reconstructive Latent-Space Neural Radiance Fields for Efficient 3D Scene Representations. *arXiv* preprint arXiv:2310.17880, 2023.
- Jonathan T. Barron, Ben Mildenhall, Dor Verbin, Pratul P. Srinivasan, and Peter Hedman. Mip-NeRF 360: Unbounded Anti-Aliased Neural Radiance Fields. In *Proceedings of the IEEE/CVF Conference on Computer Vision and Pattern Recognition (CVPR)*, pp. 5470–5479, June 2022.
- Bahri Batuhan Bilecen, Yigit Yalin, Ning Yu, and Aysegul Dundar. Reference-based 3d-aware image editing with triplanes. In *Proceedings of the Computer Vision and Pattern Recognition Conference (CVPR)*, pp. 5904–5915, June 2025.
- Adriano Cardace, Pierluigi Zama Ramirez, Francesco Ballerini, Allan Zhou, Samuele Salti, and Luigi Di Stefano. Neural Processing of Tri-Plane Hybrid Neural Fields. In *ICLR*, 2024.
- E. R. Chan, K. Nagano, M. A. Chan, A. W. Bergman, J. Park, A. Levy, M. Aittala, S. De Mello, T. Karras, and G. Wetzstein. Generative Novel View Synthesis with 3D-Aware Diffusion Models. In 2023 IEEE/CVF International Conference on Computer Vision (ICCV), pp. 4194–4206, Los Alamitos, CA, USA, oct 2023. IEEE Computer Society. doi: 10.1109/ICCV51070.2023.00389.
- Eric R. Chan, Connor Z. Lin, Matthew A. Chan, Koki Nagano, Boxiao Pan, Shalini De Mello, Orazio Gallo, Leonidas J. Guibas, Jonathan Tremblay, Sameh Khamis, Tero Karras, and Gordon Wetzstein. Efficient Geometry-Aware 3D Generative Adversarial Networks. In *Proceedings of the IEEE/CVF Conference on Computer Vision and Pattern Recognition (CVPR)*, pp. 16123–16133, June 2022.
- Angel X. Chang, Thomas Funkhouser, Leonidas Guibas, Pat Hanrahan, Qixing Huang, Zimo Li, Silvio Savarese, Manolis Savva, Shuran Song, Hao Su, et al. ShapeNet: An Information-Rich 3D Model Repository. *arXiv preprint arXiv:1512.03012*, 2015. Dataset available under the ShapeNet Terms of Use, accessible at https://shapenet.org/terms. Accessed on 2025-05-15.
- Anpei Chen, Zexiang Xu, Andreas Geiger, Jingyi Yu, and Hao Su. TensoRF: Tensorial Radiance Fields. In *European Conference on Computer Vision (ECCV)*, 2022.
- Hansheng Chen, Jiatao Gu, Anpei Chen, Wei Tian, Zhuowen Tu, Lingjie Liu, and Hao Su. Single-Stage Diffusion NeRF: A Unified Approach to 3D Generation and Reconstruction. In *Proceedings of the IEEE/CVF International Conference on Computer Vision (ICCV)*, pp. 2416–2425, October 2023.
- Sara Fridovich-Keil, Giacomo Meanti, Frederik Rahbæk Warburg, Benjamin Recht, and Angjoo Kanazawa. K-Planes: Explicit Radiance Fields in Space, Time, and Appearance. In *Proceedings of the IEEE/CVF Conference on Computer Vision and Pattern Recognition (CVPR)*, pp. 12479–12488, June 2023.
- Yicong Hong, Kai Zhang, Jiuxiang Gu, Sai Bi, Yang Zhou, Difan Liu, Feng Liu, Kalyan Sunkavalli, Trung Bui, and Hao Tan. LRM: Large Reconstruction Model for Single Image to 3D. In *The Twelfth International Conference on Learning Representations*, 2024.

- Wonbong Jang and Lourdes Agapito. CodeNeRF: Disentangled Neural Radiance Fields for Object Categories. In *Proceedings of the IEEE/CVF International Conference on Computer Vision (ICCV)*, pp. 12949–12958, October 2021.
 - Xiaoliang Ju and Hongsheng Li. Directtrigs: Triplane-based gaussian splatting field representation for 3d generation, 2025.
 - James T. Kajiya and Brian P. Von Herzen. Ray Tracing Volume Densities. SIGGRAPH Comput. Graph., 18(3):165—174, January 1984. doi: 10.1145/964965.808594.
 - Bernhard Kerbl, Georgios Kopanas, Thomas Leimkühler, and George Drettakis. 3D Gaussian Splatting for Real-Time Radiance Field Rendering. ACM Transactions on Graphics, 42(4), July 2023.
 - Umar Khalid, Hasan Iqbal, Nazmul Karim, Jing Hua, and Chen Chen. LatentEditor: Text Driven Local Editing of 3D Scenes, 2023.
 - Taekyung Ki, Dongchan Min, and Gyeongsu Chae. Learning to Generate Conditional Tri-Plane for 3D-Aware Expression Controllable Portrait Animation. In Aleš Leonardis, Elisa Ricci, Stefan Roth, Olga Russakovsky, Torsten Sattler, and Gül Varol (eds.), *Computer Vision ECCV 2024*, pp. 476–493, Cham, 2025. Springer Nature Switzerland. ISBN 978-3-031-73232-4.
 - Jumin Lee, Sebin Lee, Changho Jo, Woobin Im, Juhyeong Seon, and Sung-Eui Yoon. SemCity: Semantic Scene Generation with Triplane Diffusion. In *Proceedings of the IEEE/CVF Conference on Computer Vision and Pattern Recognition (CVPR)*, pp. 28337–28347, June 2024.
 - Ying-Tian Liu, Yuan-Chen Guo, Guan Luo, Heyi Sun, Wei Yin, and Song-Hai Zhang. PI3D: Efficient Text-to-3D Generation with Pseudo-Image Diffusion. In *Proceedings of the IEEE/CVF Conference on Computer Vision and Pattern Recognition (CVPR)*, pp. 19915–19924, June 2024.
 - Antoine Mercier, Ramin Nakhli, Mahesh Reddy, Rajeev Yasarla, Hong Cai, Fatih Porikli, and Guillaume Berger. Hexagen3d: Stablediffusion is one step away from fast and diverse text-to-3d generation. In *Proceedings of the Winter Conference on Applications of Computer Vision (WACV)*, pp. 1247–1257, February 2025.
 - Gal Metzer, Elad Richardson, Or Patashnik, Raja Giryes, and Daniel Cohen-Or. Latent-NeRF for Shape-Guided Generation of 3D Shapes and Textures. In *Proceedings of the IEEE/CVF Conference on Computer Vision and Pattern Recognition (CVPR)*, pp. 12663–12673, June 2023.
 - Ben Mildenhall, Pratul P. Srinivasan, Matthew Tancik, Jonathan T. Barron, Ravi Ramamoorthi, and Ren Ng. NeRF: Representing Scenes as Neural Radiance Fields for View Synthesis. In *ECCV*, 2020.
 - Thomas Müller, Alex Evans, Christoph Schied, and Alexander Keller. Instant Neural Graphics Primitives with a Multiresolution Hash Encoding. *ACM Trans. Graph.*, 41(4):102:1–102:15, July 2022. doi: 10.1145/3528223.3530127.
 - Michael Niemeyer and Andreas Geiger. Giraffe: Representing scenes as compositional generative neural feature fields. In *Proceedings of the IEEE/CVF Conference on Computer Vision and Pattern Recognition (CVPR)*, pp. 11453–11464, June 2021.
 - JangHo Park, Gihyun Kwon, and Jong Chul Ye. ED-NeRF: Efficient Text-Guided Editing of 3D Scene With Latent Space NeRF. In *International Conference on Learning Representations*, 2024.
 - P. Paysan, R. Knothe, B. Amberg, S. Romdhani, and T. Vetter. A 3D Face Model for Pose and Illumination Invariant Face Recognition. In *Proceedings of the 6th IEEE International Conference on Advanced Video and Signal based Surveillance (AVSS) for Security, Safety and Monitoring in Smart Environments*, Genova, Italy, 2009. IEEE. Dataset available at https://faces.dmi.unibas.ch/bfm/index.php?nav=1-1-0&id=details.Accessed on 2025-09-15.
 - Robin Rombach, Andreas Blattmann, Dominik Lorenz, Patrick Esser, and Björn Ommer. High-Resolution Image Synthesis With Latent Diffusion Models. In *Proceedings of the IEEE/CVF Conference on Computer Vision and Pattern Recognition (CVPR)*, pp. 10684–10695, June 2022.

- Antoine Schnepf, Karim Kassab, Jean-Yves Franceschi, Laurent Caraffa, Flavian Vasile, Jeremie Mary, Andrew I. Comport, and Valerie Gouet-Brunet. Bringing NeRFs to the Latent Space: Inverse Graphics Autoencoder. In *The Thirteenth International Conference on Learning Representations*, 2025.
- Katja Schwarz, Yiyi Liao, Michael Niemeyer, and Andreas Geiger. Graf: Generative radiance fields for 3d-aware image synthesis, 2021.
- Hoigi Seo, Hayeon Kim, Gwanghyun Kim, and Se Young Chun. Ditto-nerf: Diffusion-based iterative text to omni-directional 3d model. *arXiv preprint arXiv:2304.02827*, 2023.
- J. Ryan Shue, Eric Ryan Chan, Ryan Po, Zachary Ankner, Jiajun Wu, and Gordon Wetzstein. 3D Neural Field Generation Using Triplane Diffusion. In *Proceedings of the IEEE/CVF Conference on Computer Vision and Pattern Recognition (CVPR)*, pp. 20875–20886, June 2023.
- Prajwal Singh, Ashish Tiwari, Gautam Vashishtha, and Shanmuganathan Raman. C3-NeRF: Modeling Multiple Scenes via Conditional-cum-Continual Neural Radiance Fields. *arXiv preprint* arXiv:2411.19903, 2024.
- Wenqiang Sun, Zhengyi Wang, Shuo Chen, Yikai Wang, Zilong Chen, Jun Zhu, and Jun Zhang. Freeplane: Unlocking free lunch in triplane-based sparse-view reconstruction models. ArXiv, abs/2406.00750, 2024.
- Matthew Tancik, Ethan Weber, Evonne Ng, Ruilong Li, Brent Yi, Justin Kerr, Terrance Wang, Alexander Kristoffersen, Jake Austin, Kamyar Salahi, Abhik Ahuja, David McAllister, and Angjoo Kanazawa. Nerfstudio: A modular framework for neural radiance field development. In *ACM SIGGRAPH 2023 Conference Proceedings*, SIGGRAPH '23, 2023.
- Tengfei Wang, Bo Zhang, Ting Zhang, Shuyang Gu, Jianmin Bao, Tadas Baltrusaitis, Jingjing Shen, Dong Chen, Fang Wen, Qifeng Chen, and Baining Guo. RODIN: A Generative Model for Sculpting 3D Digital Avatars Using Diffusion. In *Proceedings of the IEEE/CVF Conference on Computer Vision and Pattern Recognition (CVPR)*, pp. 4563–4573, June 2023.
- Zhennan Wu, Yang Li, Han Yan, Taizhang Shang, Weixuan Sun, Senbo Wang, Ruikai Cui, Weizhe Liu, Hiroyuki Sato, Hongdong Li, and Pan Ji. BlockFusion: Expandable 3D Scene Generation using Latent Tri-plane Extrapolation. *ACM Trans. Graph.*, 43(4), July 2024. ISSN 0730-0301. doi: 10.1145/3658188.
- Han Yan, Yang Li, Zhennan Wu, Shenzhou Chen, Weixuan Sun, Taizhang Shang, Weizhe Liu, Tian Chen, Xiaqiang Dai, Chao Ma, Hongdong Li, and Pan Ji. Frankenstein: Generating Semantic-Compositional 3D Scenes in One Tri-Plane. In *SIGGRAPH Asia 2024 Conference Papers*, SA '24, New York, NY, USA, 2024. Association for Computing Machinery. ISBN 9798400711312. doi: 10.1145/3680528.3687672.
- J. Ye, N. Wang, and X. Wang. FeatureNeRF: Learning Generalizable NeRFs by Distilling Foundation Models. In 2023 IEEE/CVF International Conference on Computer Vision (ICCV), pp. 8928–8939, Los Alamitos, CA, USA, oct 2023. IEEE Computer Society. doi: 10.1109/ICCV51070. 2023.00823.
- Richard Zhang, Phillip Isola, Alexei A. Efros, Eli Shechtman, and Oliver Wang. The Unreasonable Effectiveness of Deep Features as a Perceptual Metric. In *Proceedings of the IEEE Conference on Computer Vision and Pattern Recognition (CVPR)*, June 2018.

A WORKS UTILIZING TRI-PLANES FOR TARGETED TASKS

In this section, we highlight representative works that utilize Tri-Planes for varied targeted tasks.

Editing. Bilecen et al. (2025); Ki et al. (2025) use Tri-Planes to perform 3D-aware editing, based on conditioning images. Such editing allows to combine the overall appearance of one object with selected characteristics of a different object.

Feed-forward reconstruction. Hong et al. (2024); Wang et al. (2023); Sun et al. (2024) propose feed-forward image-to-3D pipelines: they infer Tri-Planes from single images by switching the output modality of image-based models to Tri-Planes.

Generation. Shue et al. (2023); Chen et al. (2023); Anciukevičius et al. (2023) build a diffusion framework around Tri-Planes, treating them as if they were images with more channels, which enables 3D object generation using image generative models.

Classification. Cardace et al. (2024) leverage Tri-Planes to classify neural fields without recreating the explicit signal (i.e. without rendering), and highlight the rich semantic signal present in Tri-Planes, as well as their ease of use with standard neural architectures.

B ADDITIONAL IMPLEMENTATION DETAILS

This section presents some additional details regarding the training of Fused-Planes, namely its warm-up stage and the early stopping of the encoder.

In practice, we use two regimes of optimization to gain some computational efficiency. In fact, we notice that the encoder E_{ϕ} converges before the set of N=2000 Fused-Planes. Hence, continuing to optimize it would be unnecessary. As such, we jointly train the encoder only with a subset $\mathcal{T}_1 = \{T_1,...,T_{N_1}\}$ of Fused-Planes (regime 1), before learning the remaining Fused-Planes $\mathcal{T}_2 = \{T_{N_1+1},...T_N\}$ with a frozen encoder (regime 2). We set $N_1=500$. For completeness, we also detail the warm-up stage of the Fused-Planes (at the start of regimes 1 and 2). This warm-up stage is necessary just after the random initialization of Fused-Planes, to avoid back-propagating random gradients into the auto-encoder.

Regime 1. We start by warming-up \mathcal{T}_1 with the following objective:

$$\min_{\mathcal{T}_{1},\alpha} \sum_{i=1}^{N_{1}} \sum_{j=1}^{V} \mathcal{L}_{i,j}^{(\text{latent})}(\phi, T_{i}, \alpha) . \tag{8}$$

We then optimize the Fused-Planes in \mathcal{T}_1 , the encoder E_{ϕ} and the decoder D_{ψ} using Equation (7), recalled here:

$$\min_{\mathcal{T}_{1},\alpha,\phi,\psi} \sum_{i=1}^{N_{1}} \sum_{j=1}^{V} \lambda^{(\text{latent})} \mathcal{L}_{i,j}^{(\text{latent})}(\phi, T_{i}, \alpha) + \lambda^{(\text{RGB})} \mathcal{L}_{i,j}^{(\text{RGB})}(\psi, T_{i}, \alpha) + \lambda^{(\text{ae})} \mathcal{L}_{i,j}^{(\text{ae})}(\phi, \psi) .$$
(9)

Regime 2. Similarly to the first regime, we start by warming-up \mathcal{T}_2 with the following objective:

$$\min_{\mathcal{T}_{2},\alpha} \sum_{i=N,+1}^{N} \sum_{i=1}^{V} \mathcal{L}_{i,j}^{(\text{latent})}(\phi, T_{i}, \alpha) . \tag{10}$$

We then optimize the Fused-Planes in \mathcal{T}_2 , but only $\mathcal{L}^{(RGB)}$ is needed, as the encoder no longer requires training. We keep fine-tuning the decoder D_{ψ} . The objective is:

$$\min_{\mathcal{T}_2, \alpha, \psi} \sum_{i=N_1+1}^{N} \sum_{j=1}^{V} \lambda^{(\text{RGB})} \mathcal{L}_{i,j}^{(\text{RGB})}(\psi, T_i, \alpha) . \tag{11}$$

Practically, we achieve the previous objective using mini-batch gradient descent. Details can be found in Algorithm 1. The rendering quality remains the same between the two regimes, as illustrated in Tables 5 and 6.

C DATASET DETAILS

We use ShapeNet (Chang et al., 2015) and Basel-Face (Paysan et al., 2009) to evaluate the novel view synthesis performance of the object representations.

The ShapeNet dataset is a large-scale, annotated collection of 3D models covering various object categories, widely used for 3D applications. For ShapeNet objects, we render V=160 views, sampled from the upper hemisphere surrounding the object.

The Basel-Face dataset contains more than 1000 distinct face models. The faces are generated from a 3D morphable face model with 199 principle components. For faces, we take V=50 front-facing views.

 All views are rendered at a resolution of 128×128 . In all our experiments, we use 90% of the views for training and 10% for evaluation.

D SUPPLEMENTARY RESULTS

D.1 QUALITATIVE RESULTS

We present in Figures 7 to 11 additional qualitative comparisons across all the methods discussed in our experiments (Section 4). Fused-Plane demonstrates similar visual quality to state-of-the-art methods.

D.2 QUANTITATIVE RESULTS

Regarding rendering quality, we present per-scene NVS metrics in Tables 9 to 13.

Regarding resource costs, the shared components (i.e. encoder, decoder and base planes) of Fused-Planes and Fused-Planes-ULW respectively require a total of 360.75 MB and 384.19 MB of storage capacity. Note that we do not include the memory footprint of these components in our analysis, as this overhead is constant regardless of the number of objects, and hence negligible in large-scale settings. This memory cost is illustrated in Figure 4 and magnified in Figure 6, focusing on the range [0,100].

Table 5: **Quantitative comparison.** NVS performances on ShapeNet Cars in both regimes of our training.

			Shapel	Net	Cars		
		Regime 1				Regime 2	
	PSNR↑	SSIM↑	LPIPS↓		PSNR↑	SSIM↑	LPIPS↓
Tri-Planes (RGB) Fused-Planes	28.49 28.14	0.9539 0.9505	0.0291 0.0301		28.58 28.77	0.9505 0.9496	0.0360 0.0383

Table 6: **Quantitative comparison.** NVS performances on Basel Faces in both regimes of our training.

			Base	l F	aces		
		Regime 1				Regime 2	
	PSNR↑	SSIM↑	LPIPS↓		PSNR↑	SSIM↑	LPIPS↓
Tri-Planes (RGB) Fused-Planes	36.82 36.17	0.9807 0.9678	0.0122 0.0062		36.35 36.99	0.9787 0.9712	0.0129 0.0056

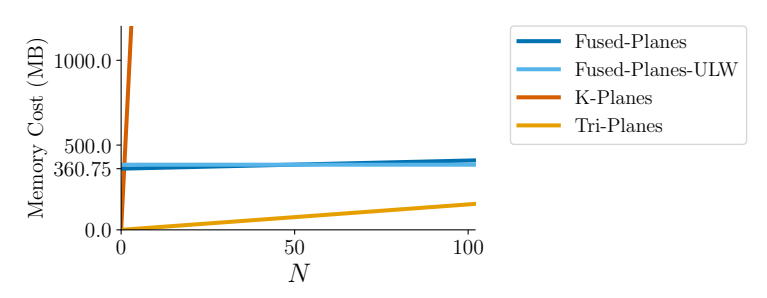


Figure 6: **Memory costs.** This figure presents the memory costs depicted in Figure 4 within the range $N \in [0, 100]$.

D.3 MEMORY BREAKDOWN

Table 7 provides a breakdown of the memory footprint of the different components used. The memory cost required by a single object is notably low compared to our baselines in the main paper. The memory cost required by our shared components can be considered as an acceptable entry cost, as its value is less than a single K-Planes representation.

Table 7: **Memory breakdown.** This table breaks down the memory footprints of the different components in our pipeline. Note that the memory usage of shared components remains constant and does not depend on the number of objects. In contrast, the memory footprint for storing objects *increases linearly* with the number of objects. Therefore, in large-scale settings, the dominant factor is the memory that *increases* with the number of objects, as illustrated in Figure 4.

Module	Shared?	Size
Encoder E_{ϕ}	✓	130.38 MB
Decoder D_{ψ}	✓	178.86 MB
$50 \times$ base planes $\mathcal{B}(F^{\text{mac}} = 22)$	✓	51.5 MB
$1 \times \text{tiny MLP (renderer } R_{\alpha})$	✓	14.27 KB
$1 \times \text{ micro plane } T_i^{\text{mic}} (F^{\text{mic}} = 10)$	X	480 KB
$1 imes$ weight W_i	X	811 B
Memory footprint of shared components	✓	360.75 MB
Memory footprint of a single object	X	0.481 MB

E CODENERF-A

CodeNeRF. CodeNeRF (Jang & Agapito, 2021) learns a set of scenes with a single neural representation f_{θ} which is conditioned on scene-specific latent codes. Specifically, for each scene, a shape code z_s and an appearance code z_a is learned, such that $f_{\theta}(z_s, z_a)$ models the current scene. Once the conditional NeRF f_{θ} is trained on a large set of scenes, it can learn new scenes using

 test-time optimization. This test-time optimization consists of learning a new scene by optimizing only the codes (z_s,z_a) , while keeping f_θ fixed. By reducing the number of trainable parameters, test-time-optimization offers increased training speed. Furthermore, the memory required to store an additional scene on disk is very low, since only (z_s,z_a) need to be stored.

CodeNeRF-A. In our experiments, we introduce CodeNeRF-A as a new comparative baseline. CodeNeRF-A employs a novel training procedure inspired by ours, which leverages the test-time optimization method originally proposed by CodeNeRF to improve efficiency for learning multiple scenes. Specifically, we first train the shared neural representation f_{θ} of CodeNeRF on a subset O_1 of $\mathcal O$ composed of N_1 scenes. Subsequently, we employ test-time-optimization with the previously trained representation to learn the remaining scenes O_2 , with lowered training times.

We present in Table 8 a comparison of CodeNeRF-A performances when taking $N_1=500$ and $N_1=1000$. CodeNeRF-A showcases better performances with $N_1=1000$, which we set throughout the paper for this method.

Table 8: Choice of N_1 for CodeNeRF-A. CodeNeRF-A showcases better performances when taking $N_1 = 1000$, which we set throughout the paper for this method.

	N_1	Sha	peNet data	E	Basel Faces				
	111	PSNR	SSIM	LPIPS	PSNR	SSIM	LPIPS		
CodeNeRF-A CodeNeRF-A	500 1000	26.81 26.99	0.9108 0.9154	0.1281 0.1257	34.15 35.44	0.964 0.971	0.011 0.010		

F HYPERPARAMETERS

For reproducibility purposes, Tables 14 and 15 expose our hyperparameter settings respectively for the first and second regimes of our training. A more detailed list of our hyperparameters can be found in the configuration files of our open-source code.

Table 9: Per-object quantitative comparison on Basel Faces.

	Planar		Face 1			Face 2			Face 3			Face 4	
	Fianai	PSNR	SSIM	LPIPS									
Vanilla-NeRF	Х	43.44	0.996	0.001	43.90	0.997	0.001	42.65	0.996	0.001	41.64	0.994	0.003
Instant-NGP	X	37.79	0.987	0.004	40.01	0.990	0.002	35.38	0.977	0.013	32.96	0.969	0.016
TensoRF	X	40.80	0.993	0.003	42.72	0.995	0.001	40.96	0.993	0.003	38.16	0.982	0.011
3DGS	X	43.69	0.998	0.001	45.41	0.998	0.001	43.22	0.997	0.001	39.93	0.986	0.007
CodeNeRF	Х	35.49	0.974	0.009	36.35	0.974	0.006	34.42	0.970	0.012	35.60	0.971	0.012
CodeNeRF-A	X	36.25	0.974	0.008	37.14	0.977	0.005	32.49	0.961	0.015	35.87	0.972	0.013
K-Planes	1	40.68	0.993	0.003	39.46	0.988	0.010	41.11	0.993	0.004	39.68	0.990	0.004
Tri-Planes	✓	36.05	0.978	0.015	37.46	0.982	0.011	36.78	0.980	0.014	35.59	0.977	0.012
Fused-Planes-ULW	√	33.84	0.950	0.013	35.00	0.958	0.007	33.41	0.959	0.011	33.58	0.954	0.010
Fused-Planes	✓	36.24	0.970	0.007	38.63	0.975	0.004	37.04	0.975	0.006	37.04	0.971	0.006

Table 10: Per-object quantitative comparison on ShapeNet Cars.

	Planar		Car 1			Car 2			Car 3			Car 4	
	1 Ianai	PSNR	SSIM	LPIPS									
Vanilla-NeRF	Х	38.43	0.995	0.003	41.20	0.995	0.005	37.43	0.994	0.005	39.53	0.995	0.003
Instant-NGP	X	35.31	0.986	0.008	37.88	0.990	0.010	34.06	0.987	0.013	36.33	0.989	0.007
TensoRF	X	38.66	0.994	0.003	40.55	0.995	0.005	37.80	0.995	0.004	40.00	0.995	0.003
3DGS	X	32.00	0.966	0.057	38.74	0.993	0.010	35.41	0.985	0.024	37.51	0.994	0.006
CodeNeRF	Х	27.87	0.950	0.055	28.05	0.937	0.097	26.19	0.929	0.088	27.07	0.930	0.075
CodeNeRF-A	X	27.10	0.946	0.055	26.86	0.929	0.103	25.25	0.921	0.092	27.10	0.932	0.074
K-Planes	/	30.51	0.966	0.029	33.84	0.976	0.027	29.73	0.968	0.037	30.57	0.967	0.031
Tri-Planes	✓	30.11	0.962	0.024	30.13	0.949	0.043	28.86	0.949	0.040	29.67	0.950	0.039
Fused-Planes-ULW	✓	27.60	0.938	0.054	29.91	0.948	0.064	28.44	0.945	0.050	28.87	0.942	0.051
Fused-Planes	✓	30.15	0.964	0.021	31.20	0.961	0.043	29.69	0.958	0.035	30.05	0.954	0.033

Table 11: Per-object quantitative comparison on ShapeNet Sofas.

	Planar		Sofa 1			Sofa 2			Sofa 3			Sofa 4	
	1 Ianai	PSNR	SSIM	LPIPS									
Vanilla-NeRF	Х	31.06	0.966	0.034	31.83	0.965	0.032	33.58	0.940	0.122	36.82	0.984	0.013
Instant-NGP	X	29.91	0.969	0.031	33.60	0.975	0.027	35.42	0.974	0.013	35.54	0.977	0.016
TensoRF	X	32.92	0.987	0.011	37.17	0.992	0.010	37.47	0.987	0.009	37.98	0.987	0.013
3DGS	X	30.85	0.986	0.020	33.95	0.989	0.025	34.60	0.982	0.023	33.46	0.984	0.047
CodeNeRF	Х	25.47	0.938	0.113	29.80	0.938	0.068	29.18	0.919	0.139	30.14	0.944	0.100
CodeNeRF-A	X	24.61	0.928	0.121	29.67	0.936	0.067	28.05	0.899	0.130	29.39	0.938	0.092
K-Planes	✓	25.84	0.947	0.054	32.28	0.974	0.028	32.90	0.968	0.028	32.59	0.964	0.037
Tri-Planes	✓	26.34	0.929	0.082	29.24	0.930	0.091	28.89	0.903	0.121	29.43	0.922	0.118
Fused-Planes-ULW	✓	24.72	0.921	0.130	30.29	0.938	0.047	29.99	0.917	0.091	31.06	0.947	0.069
Fused-Planes	✓	27.83	0.964	0.020	31.75	0.958	0.024	31.71	0.945	0.032	32.39	0.963	0.038

Table 12: Per-object quantitative comparison on ShapeNet Speakers.

	Planar		Speaker 1			Speaker 2	2		Speaker 3	3		Speaker 4	1
	1 Ianai	PSNR	SSIM	LPIPS									
Vanilla-NeRF	Х	35.95	0.962	0.065	30.97	0.980	0.021	35.41	0.970	0.032	33.65	0.977	0.015
Instant-NGP	X	36.56	0.983	0.016	27.31	0.955	0.043	34.75	0.980	0.024	31.16	0.966	0.022
TensoRF	X	38.73	0.989	0.012	29.74	0.978	0.024	37.57	0.988	0.017	33.60	0.976	0.016
3DGS	X	34.45	0.981	0.059	24.21	0.870	0.095	31.70	0.979	0.071	28.11	0.940	0.071
CodeNeRF	Х	29.81	0.894	0.133	24.91	0.931	0.106	28.85	0.925	0.178	28.26	0.935	0.126
CodeNeRF-A	X	23.73	0.875	0.167	24.32	0.922	0.114	27.31	0.905	0.184	26.11	0.918	0.129
K-Planes	√	33.80	0.969	0.034	21.84	0.905	0.102	32.33	0.963	0.046	27.19	0.923	0.069
Tri-Planes	✓	29.25	0.911	0.147	23.11	0.903	0.098	29.30	0.914	0.160	26.41	0.907	0.132
Fused-Planes-ULW	✓	30.38	0.932	0.134	26.75	0.948	0.049	29.93	0.940	0.104	29.83	0.942	0.063
Fused-Planes	/	32.89	0.966	0.042	26.40	0.949	0.046	30.63	0.951	0.066	30.04	0.947	0.057

Table 13: Per-object quantitative comparison on ShapeNet Furnitures.

	Planar	Furniture 1			1	Furniture 2			Furniture 3			Furniture 4		
		PSNR	SSIM	LPIPS										
Vanilla-NeRF	Х	38.42	0.976	0.014	35.56	0.985	0.015	38.01	0.978	0.018	35.75	0.965	0.028	
Instant-NGP	X	35.12	0.951	0.032	33.64	0.977	0.023	33.91	0.954	0.035	34.49	0.959	0.031	
TensoRF	X	38.03	0.974	0.018	36.23	0.989	0.013	36.22	0.973	0.021	35.23	0.964	0.031	
3DGS	X	34.49	0.991	0.033	31.14	0.989	0.051	33.15	0.975	0.050	33.49	0.998	0.052	
CodeNeRF CodeNeRF-A	X X	29.82 28.65	0.909 0.868	0.157 0.156	27.22 26.18	0.928 0.914	0.139 0.148	30.20 28.47	0.932 0.899	0.224 0.234	30.68 29.11	0.944 0.918	0.139 0.146	
K-Planes Tri-Planes	1	34.41 26.88	0.951 0.875	0.028 0.175	30.72 27.17	0.960 0.913	0.044 0.180	33.01 28.05	0.949 0.902	0.045 0.237	32.51 27.58	0.941 0.886	0.055 0.250	
Fused-Planes-ULW Fused-Planes	1	25.80 30.19	0.891 0.962	0.219 0.030	29.91 30.54	0.947 0.957	0.073 0.039	29.67 29.81	0.938 0.947	0.173 0.102	31.20 32.34	0.958 0.972	0.102 0.042	

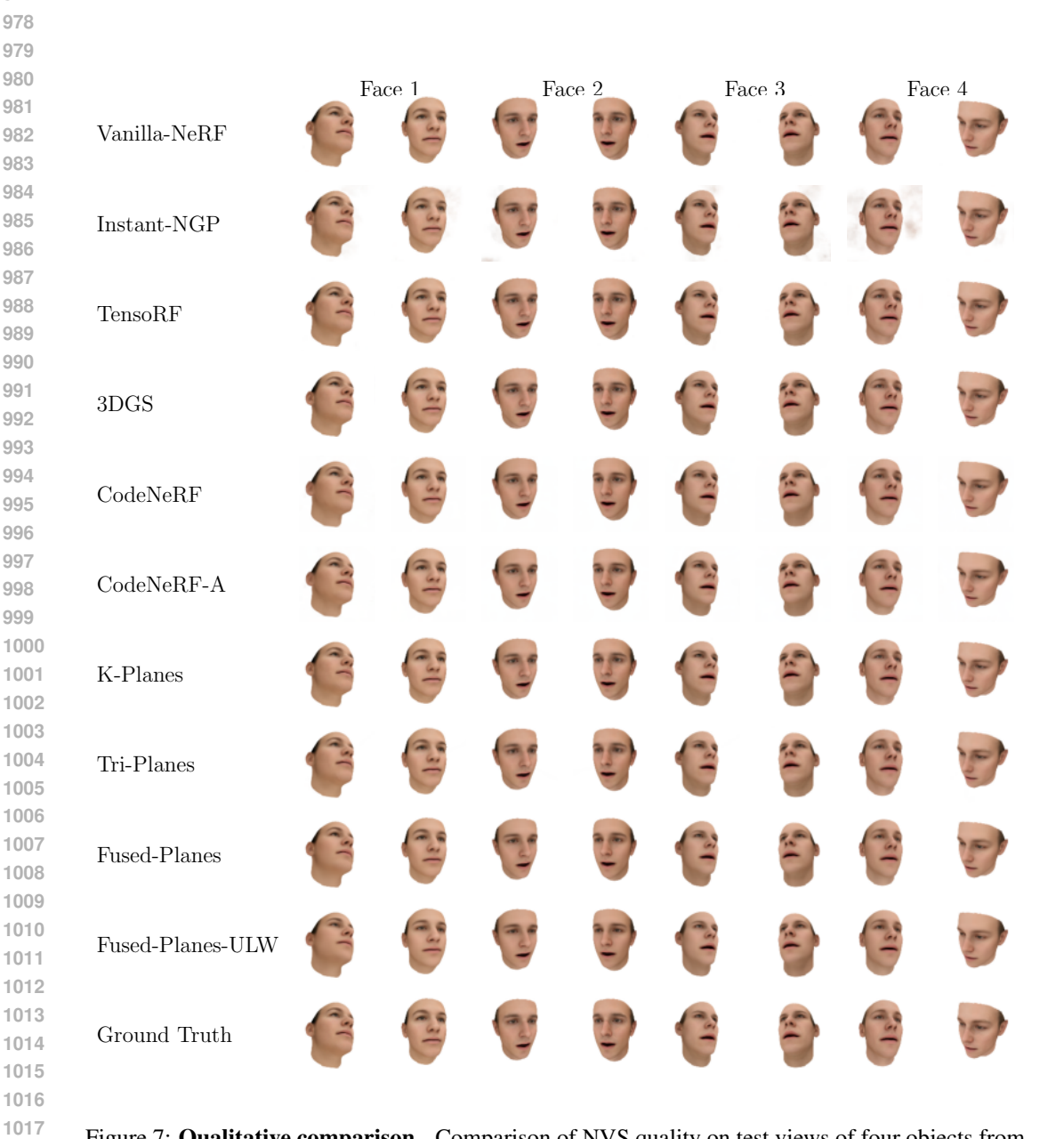


Figure 7: Qualitative comparison. Comparison of NVS quality on test views of four objects from Basel Faces.

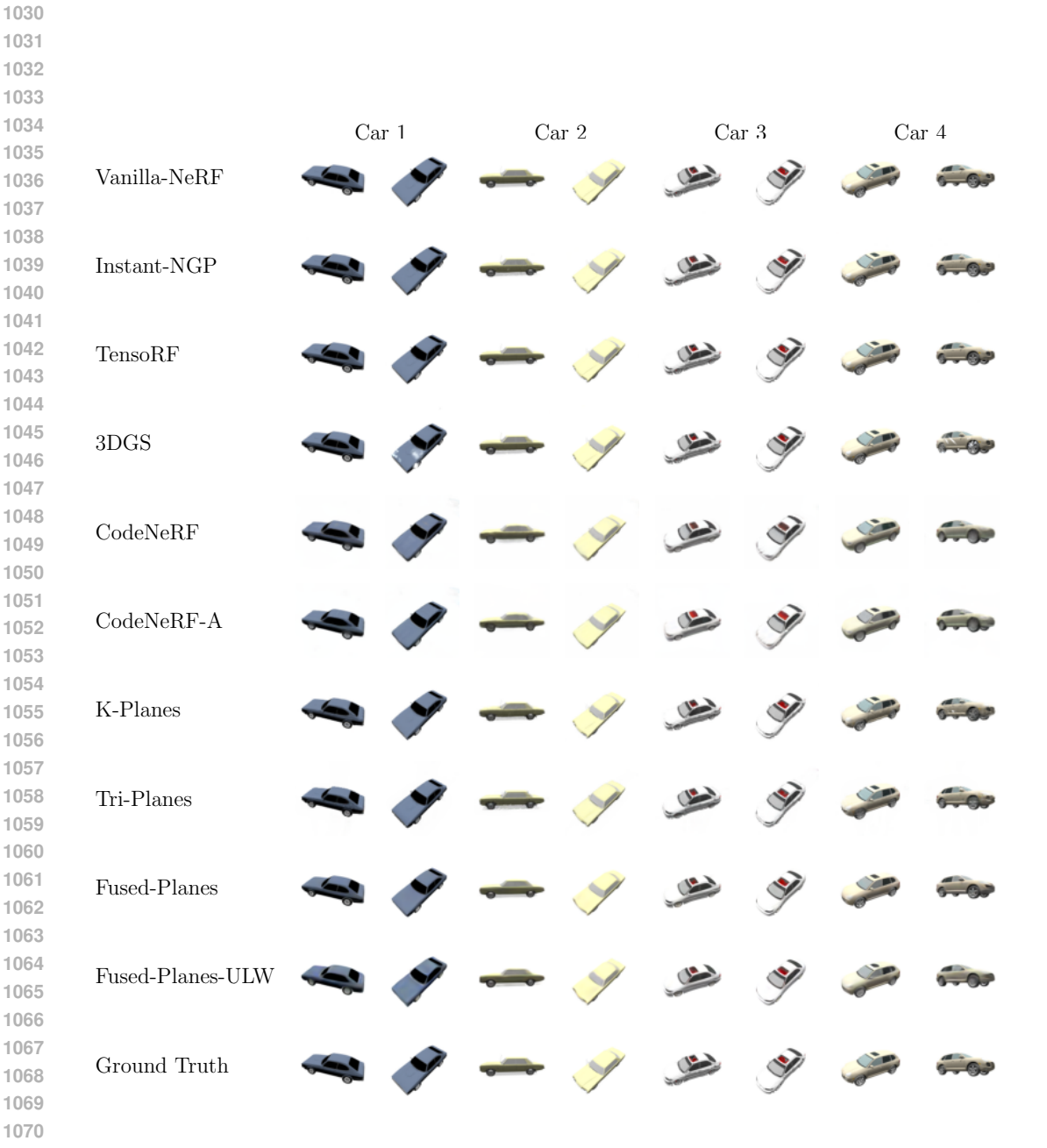


Figure 8: **Qualitative comparison.** Comparison of NVS quality on test views of four objects from the Cars category of ShapeNet.

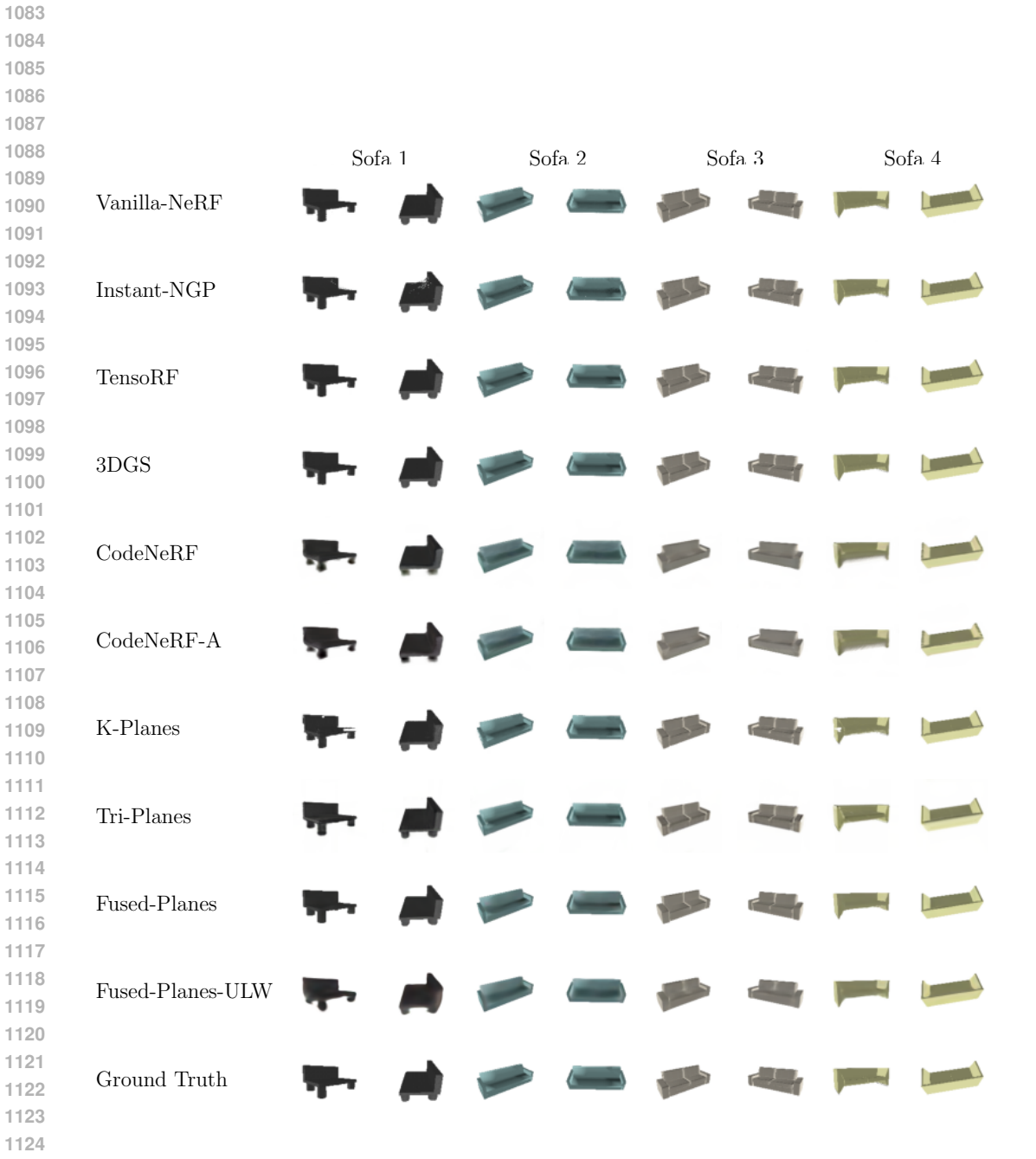


Figure 9: **Qualitative comparison.** Comparison of NVS quality on test views of four objects from the Sofas category of ShapeNet.

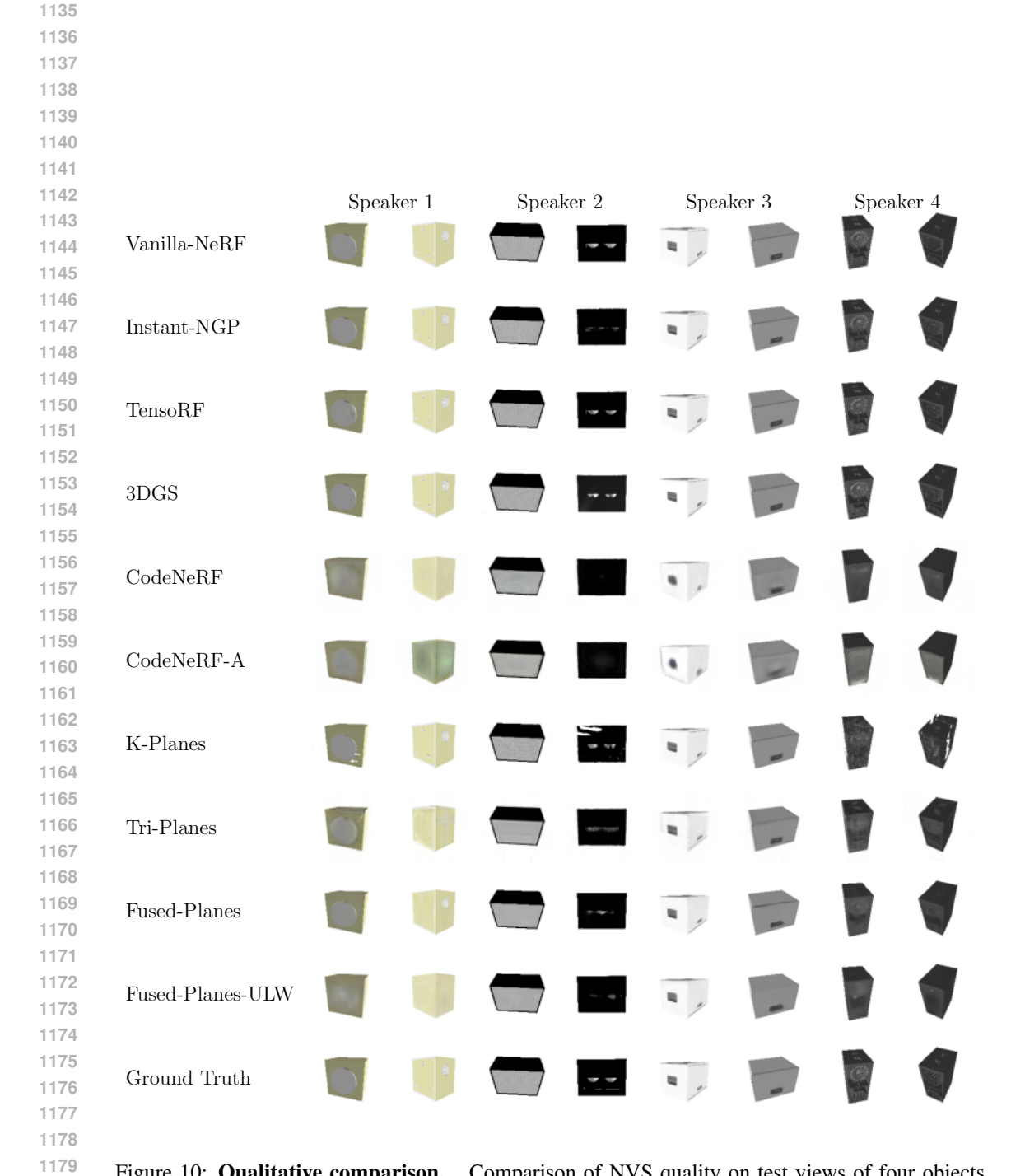


Figure 10: **Qualitative comparison.** Comparison of NVS quality on test views of four objects from the Speakers category of ShapeNet.

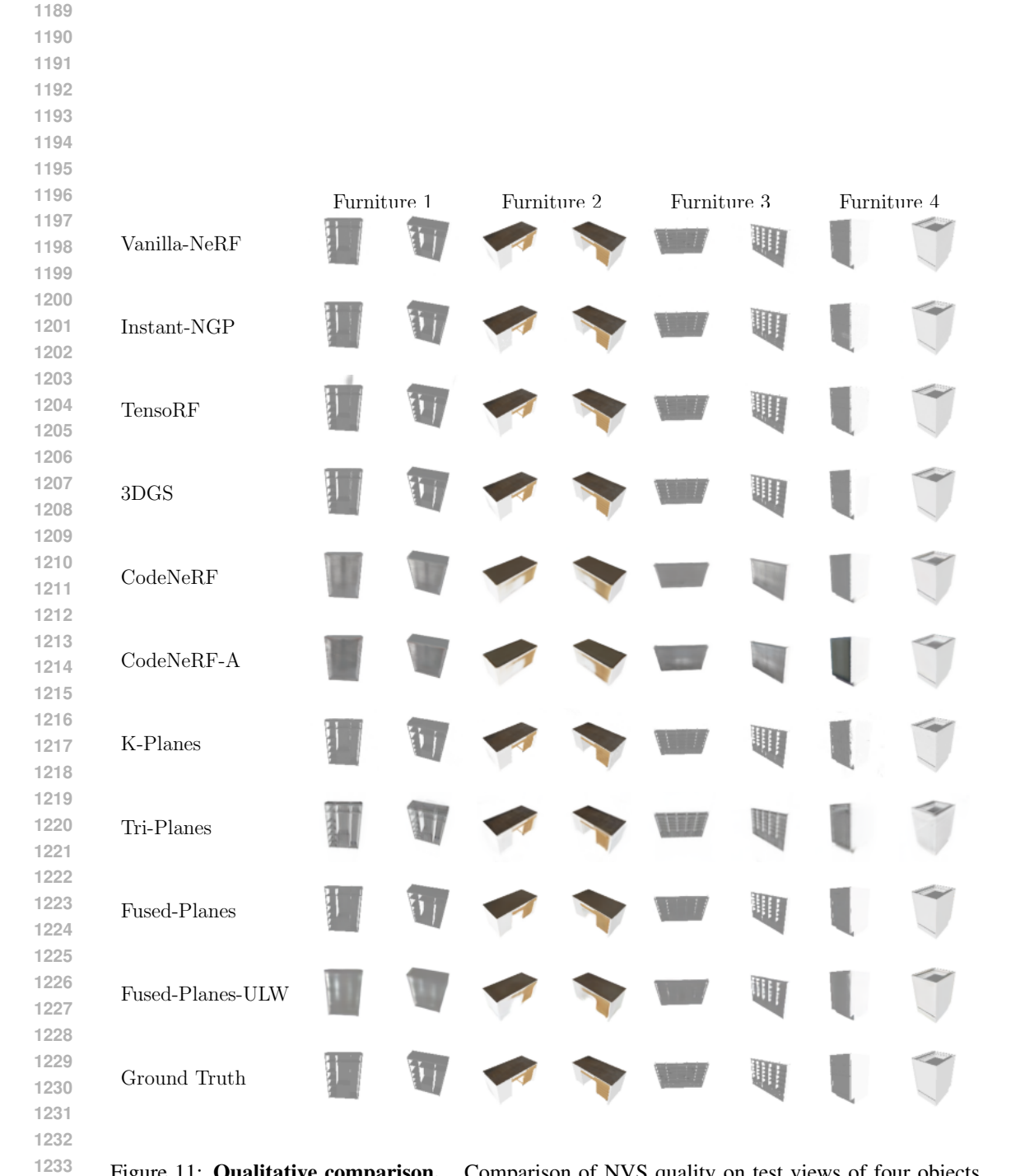


Figure 11: **Qualitative comparison.** Comparison of NVS quality on test views of four objects from the Furniture category of ShapeNet.

we aim to improve upon the resource costs

Table 14: Fused-Planes regime 1 hyperparameters.

Parameter	Value
General	
Number of scenes N	2000
Number of scenes for regime 1 N_1	500
Pretraining epochs	50
Number of epochs $N_{\rm epoch}^{(1)}$	50
Fused-Planes	
Number of micro feature $F_{\rm mic}$	10
Number of macro feature $F_{ m mac}$	22
Number of base plane M	50
Tri-Planes resolution	64
Loss	
$\lambda^{ m (latent)}$	1
$\lambda^{ m (RGB)}$	1
$\lambda^{ m (ae)}$	0.1
Optimization (warm-up)	
Optimizer	Adam
Batch size	512
Learning rate (Micro planes $T_i^{(\text{mic})}$)	10^{-2}
Learning rate (Renderer R_{α})	10^{-2}
Learning rate (Weights W_i)	10^{-2}
Learning rate (Base planes B_k)	10^{-2}
Scheduler	Multistep
Decay factor	0.3
Decay milestones	[20, 40]
Optimization (training)	
Optimizer	Adam
Batch size	32
Learning rate (encoder)	10^{-4}
Learning rate (decoder)	10^{-4}
Learning rate (Micro planes $T_i^{(\text{mic})}$)	10^{-4}
Learning rate (Renderer R_{α})	10^{-4}
Learning rate (Weights W_i)	10^{-2}
Learning rate (Base planes B_k)	10^{-2}
Scheduler	Multistep
Decay factor	0.3
Decay milestones	[20, 40]

Table 15: Fused-Planes regime 2 hyperparameters.

Parameter	Value					
General						
Number of scenes N	2000					
Number of epochs $N_{\rm epoch}^{(2)}$	80					
Number of warm-up epochs $N_{ m epoch}^{ m (WU)}$	30					
Fused-Planes						
Number of micro feature $F_{\rm mic}$	10					
Number of macro feature $F_{\rm mac}$	22					
Number of base plane M	50					
Tri-Planes resolution	64					
Loss						
$\lambda^{(latent)}$	1					
$\lambda^{ m (RGB)}$	1					
Optimization (Warm-up)						
Optimizer	Adam					
Batch size	32					
Learning rate (Micro planes $T_i^{(mic)}$)	10^{-2}					
Learning rate (Renderer R_{α})	10^{-2}					
Learning rate (Weights W_i)	10^{-2}					
Learning rate (Base planes B_k)	10^{-2}					
Scheduler	Exponential decay					
Decay factor	0.941					
Optimization (Training)						
Optimizer	Adam					
Batch size	32					
Learning rate (decoder)	10^{-4}					
Learning rate (Micro planes $T_i^{(\text{mic})}$)	10^{-3}					
Learning rate (Renderer R_{α})	10^{-3}					
Learning rate (Weights W_i)	10^{-2}					
Learning rate (Base planes B_k)	10^{-2}					
Scheduler	Exponential decay					
Decay factor	0.941					

```
1350
1351
               Algorithm 1 Training a large set of scenes.
1352
                 1: Input: \mathcal{O}, N, N_1, V, E_{\phi}, D_{\psi}, \mathcal{R}_{\alpha}, N_{\mathrm{epoch}}^{(1)}, N_{\mathrm{epoch}}^{(2)}, N_{\mathrm{epoch}}^{(\mathrm{WU})}, \lambda^{(\mathrm{latent})}, \lambda^{(\mathrm{RGB})}, \lambda^{(\mathrm{ae})}, optimizer
1353
                 2: Random initialization: \mathcal{T}^{\mathrm{mic}}, W, \mathcal{B}
1354
1355
                 4: // First N_1 = 500 objects (regime 1)
1356
                 5: for N_{\text{epoch}}^{(1)} steps do
1357
1358
                           for (i,j) in shuffle ([1,N_1] \times [1,V]) do
                 7:
                               // Compute Micro-Macro Planes
1359
                               T_i^{(\text{mic})}, T_i^{(\text{mac})} \leftarrow \mathcal{T}^{(\text{mic})}[i], W_i \mathcal{B}
                 8:
1360
                               T_i \leftarrow T_i^{(\text{mic})} \oplus T_i^{(\text{mac})}
1361
                 9:
1362
                               // Encode, Render & Decode
                10:
                               x_{i,j}, c_{i,j} \leftarrow \mathcal{O}[i][j]
1363
                               z_{i,j} \leftarrow E_{\phi}(x_{i,j})
1364
                               \tilde{z}_{i,j} \leftarrow \mathcal{R}_{\alpha}(T_i, c_{i,j})
1365
                               \hat{x}_{i,j}, \tilde{x}_{i,j} \leftarrow D_{\psi}(z_{i,j}), D_{\psi}(\tilde{z}_{i,j})
               14:
1366
               15:
                               // Compute losses
                               L_{i,j}^{(\text{latent})} \leftarrow \|z_{i,j} - \tilde{z}_{i,j}\|_2^2
1368
                               L_{i,j}^{(\text{RGB})} \leftarrow \|x_{i,j} - \tilde{x}_{i,j}\|_{2}^{2}
1369
               17:
                               L_{i,j}^{(ae)} \leftarrow \|x_{i,j} - \hat{x}_{i,j}\|_2^2
1370
               18:
1371
                               L_{i,j} \leftarrow \lambda^{(\text{latent})} L_{i,j}^{(latent)} + \lambda^{(\text{RGB})} L_{i,j}^{(RGB)} + \lambda^{(\text{ae})} L_{i,j}^{(ae)}
               19:
1372
               20:
                               // Backpropagate
1373
                               T_i^{(\text{mic})}, W_i, \mathcal{B}, \alpha, \phi, \psi \leftarrow \text{optimizer.step}(L_{i,j})
               21:
1374
               22:
                           end for
1375
               23: end for
1376
               24:
1377
               25: // Remaining objects (regime 2)
1378
               26: E_{\phi}.freeze()
1379
               27: epoch=1
               28: for N_{\rm epoch}^{(2)} steps do
1380
1381
               29:
                           for (i, j) in shuffle([\![N_1 + 1, N]\!] \times [\![1, V]\!]) do
               30:
                               // Compute Micro-Macro Planes
1383
                               T_i^{(\text{mic})}, T_i^{(\text{mac})} \leftarrow \mathcal{T}^{(\text{mic})}[i], W_i \mathcal{B}T_i \leftarrow T_i^{(\text{mic})} \oplus T_i^{(\text{mac})}
               31:
1384
               32:
1385
                               // Encode, Render & Decode
1386
                               x_{i,j}, c_{i,j} \leftarrow \mathcal{O}[i][j]
1387
                               z_{i,j} \leftarrow E_{\phi}(x_{i,j})
1388
                               \tilde{z}_{i,j} \leftarrow \mathcal{R}_{\alpha}(T_i, c_{i,j})
               36:
1389
                               \tilde{x}_{i,j} \leftarrow D_{\psi}(\tilde{z}_{i,j})
               37:
1390
               38:
                               if epoch \leq N_{
m epoch}^{
m (WU)} then
1391
               39:
               40:
                                    // Warm-up
1392
                                    L_{i,j}^{(\text{latent})} \leftarrow \|z_{i,j} - \tilde{z}_{i,j}\|_2^2
1393
               41:
1394
                                    T_i^{(\text{mic})}, W_i, \mathcal{B}, \alpha \leftarrow \text{optimizer.step}(L_{i,j}^{(\text{latent})})
               42:
1395
               43:
1396
               44:
                                   // Training
                                    L_{i,j}^{(\text{RGB})} \leftarrow \|x_{i,j} - \tilde{x}_{i,j}\|_2^2
1397
               45:
1398
                                    T_i^{(\text{mic})}, W_i, \mathcal{B}, \alpha, \psi \leftarrow \text{optimizer.step}(L_{i,i}^{(\text{RGB})})
               46:
1399
               47:
                               end if
1400
                           end for
               48:
1401
                           epoch \leftarrow epoch + 1
1402
               50: end for
```